A&A, 710, A3 (2026)
https://doi.org/10.1051/0004-6361/202558039

Astronomy & Astrophysics

The meteorite analogs of (65803) Didymos and implications for its origin

Ruoyu Zhai[1,2], Tianyi Xu[1], Liuming Peng[3], Azeem Khalid[1,2], Siyuan Li[1,2], Min Shu[3,4], and Yunzhao Wu[1,3,⋆]

[1] Purple Mountain Observatory, Chinese Academy of Sciences, Nanjing 210023, China
[2] School of Astronomy and Space Science, University of Science and Technology of China, Hefei 230026, China
[3] State Key Laboratory of Lunar and Planetary Sciences, Macau University of Science and Technology, Macau, China
[4] School of Mathematics and Information Science, Xiangnan University, Chenzhou 423000, China

Received 9 November 2025 / Accepted 14 April 2026

ABSTRACT

Context. Identifying meteorite analogs of asteroids is key to understanding their origin and evolution, evaluating planetary defense, and exploring potential space resources. The Didymos binary asteroid system, whose satellite Dimorphos was impacted by the Double Asteroid Redirection Test (DART) mission and will be further investigated by Hera, remains debated in terms of its meteorite analog. In addition, few studies have linked the spectral variations caused by the DART impact to meteorite analogs.
Aims. This study determines the mineralogical composition and meteorite analog of the Didymos system. It also seeks to investigate the differences between the spectral effects of grain size and space weathering among different types of meteorites, and to use these relationships to interpret the spectral variations observed in the Didymos system.
Methods. We used self-established calibration equations to infer the surface composition of Didymos from its spectral data. Band parameters and mineralogical parameters were derived and compared with meteorite samples.
Results. The derived band parameters and mineralogical estimates indicate that Didymos is most consistent with L ordinary chondrites, favoring type 6, with an LL subtype being less likely. For H and L chondrites, ratio spectra can help assess whether the slope variations in the asteroid system or surface are primarily dominated by the grain size effect. However, for LL chondrites, the situation is more complex, as these two effects cannot be easily distinguished. The spectrum-estimated exposure age of Didymos (~0.39 Myr) is consistent with the surface crater retention age of Dimorphos.
Conclusions. Didymos most likely originates from the highly metamorphosed inner regions of the L chondrite parent body. Based on this identification, the spectral variations in the Didymos system are interpreted as being dominated by space weathering rather than by grain size or compositional differences. The exposure age of Didymos further supports a rotational fission origin for the binary system.

Key words. techniques: spectroscopic – meteorites, meteors, meteoroids – minor planets, asteroids: general – minor planets, asteroids: individual: (65803) Didymos

1. Introduction

Identifying the meteorite analogs and mineral compositions of asteroids contributes to our understanding of their origin and evolution. Moreover, such information is essential for planning and evaluating planetary defense missions, as it provides insights into key physical properties of asteroids, such as density, strength, and porosity. It is also valuable for exploring potential space resources. However, as the target of the DART and Hera missions, the meteorite analog of the Didymos system remains under debate (Dunn et al. 2013; Ieva et al. 2024; Rivkin et al. 2023; Polishook et al. 2023; Ieva et al. 2022). Didymos system exhibits characteristics of an S-type asteroid (de León et al. 2006, 2010), and its meteorite analog is considered to be ordinary chondrites (Dunn et al. 2013). Nevertheless, the specific subtype (H, L, or LL) and the precise petrologic type are still debated.

Ordinary chondrites are primarily composed of minerals such as olivine (ol), orthopyroxene (opx), clinopyroxene (cpx), plagioclase, kamacite and taenite. They are classified into three groups – H, L, and LL – based on the abundance of Fe and the ratio of metallic iron (Fe^0) to oxidized iron (FeO), with H chondrites having the highest Fe and highest Fe^0/FeO ratios, and LL chondrites the lowest (Weisberg et al. 2006). In equilibrated ordinary chondrites (petrologic types 4–6), the fayalite (Fa) content in olivine and ferrosilite (Fs) content in low-Ca pyroxene show good homogeneity. For each subtype, these two mineralogical parameters fall within distinct, non-overlapping ranges, allowing them to be distinguished (Brearley & Jones 1998). In addition, Dunn et al. (2010b) found that the ol/(ol + px) (ratio of olivine to olivine + pyroxene) for each subtype falls within a certain range, and that combining ol/(ol + px) with Fa and Fs enables the meteorite subtype to be determined.

Visible and near-infrared (VNIR) spectroscopy is an effective method of determining the mineral composition of meteorites and asteroids (Reddy et al. 2015; Gaffey et al. 2002). The absorption features of olivine and pyroxene near 1 μm (Band I) and 2 μm (Band II) are diagnostic characteristics of ordinary chondrites. Olivine exhibits a broad and asymmetric absorption feature near 1 μm, which is composed of three overlapping absorption peaks and is caused by Fe^{2+} ions in the M1 and M2 sites of the olivine crystal lattice (Burns 1970). With increasing fayalite content (mol% Fa), the absorption band shifts toward longer wavelengths (King & Ridley 1987). The pyroxenes in ordinary chondrites are type B pyroxenes; namely, low-calcium pyroxenes, pigeonites, and lower-calcium-content high-calcium pyroxenes. These pyroxenes are characterized by narrow and

⋆ Corresponding author: wu@pmo.ac.cn

symmetric absorption bands near 1 μm and 2 μm, caused by Fe^{2+} located in the M2 site. As Ca^{2+} and Fe^{2+} substitute for Mg^{2+} in the lattice, the two absorption band centers of pyroxene shift toward longer wavelengths (Adams 1974; Burns et al. 1972; Cloutis 1985). Cloutis et al. (1986) measured the reflectance spectra of olivine-orthopyroxene mixtures and correlated the band area ratio (BAR) with opx/(ol + opx). Based on the spectra and mineral compositions of 48 ordinary chondrites, Dunn et al. (2010a,b,c) derived calibration equations relating ol/(ol + px) to the BAR, and Fa and Fs to the Band I center (BIC). Mineralogical parameters derived from band parameters can be compared with the compositional ranges of the three subtypes of ordinary chondrites to identify the specific meteoritic analog subtype.

Different band parameter analysis (BPA) methods, such as variations in the selection of red and blue edges or in the definition of band centers, can lead to inconsistencies in the calculated band parameters (Lindsay et al. 2016; Wu et al. 2018; Mitchell et al. 2020; Sanchez et al. 2020). Therefore, it is important to establish and apply self-consistent calibration equations (McClure & Lindsay 2022). Moreover, the ordinary chondrite samples used to establish the previous calibration equations were relatively limited, and samples containing both spectral and mineralogical information are difficult to obtain. Expanding the sample set would improve constraints on their mineralogical characteristics and yield more accurate results (McClure & Lindsay 2022).

Equally noteworthy is that effects such as space weathering, grain size, and compositional differences can significantly modify the spectral characteristics, thereby influencing the derived composition. Therefore, the spectral variations induced by the DART impact have also attracted wide attention from researchers (Polishook et al. 2023). At the same time, distinguishing between the effects of space weathering and grain size among different meteorite analogs remains challenging when relying solely on spectral data (MacLennan et al. 2024).

In this study, we first analyzed the spectral changes of the Didymos system before and after the DART impact, and compared the effects of grain size and space weathering across different meteorite analogs. A large dataset of meteorite spectra and their corresponding mineralogical parameters was then compiled to derive new mineralogical calibration equations. These equations were subsequently applied to determine the mineralogical compositions and meteorite analogs of the Didymos surface and the ejecta from Dimorphos. These results provide new insights into the origin and evolution of the Didymos system and contribute to assessing the effects of the DART impact.

2. Data and methodology

2.1. Spectral observations of the Didymos system

Seven VNIR spectra of the Didymos system reported by Polishook et al. (2023) were used in this study (Fig. 1). These spectra were obtained with the NASA Infrared Telescope Facility (IRTF) and SpeX (Rayner et al. 2003) during seven consecutive nights, spanning from September 26 (the night before the DART impact) through October 2, 2022. For convenience, they are hereafter referred to by their observation dates as 0926, 0927, 0928, 0929, 0930, 1001, and 1002. In addition, the VNIR spectrum of Didymos acquired in 2004 by de León et al. (2006) is shown in Fig. 1 for comparison. All spectra were normalized at 0.77 μm.

The IRTF/SpeX observational range nominally spans 0.7–2.45 μm, but the 0.7–0.8 μm region is sometimes unreliable; therefore, the usable wavelength range must be defined according to the specific observation (Polishook, priv. comm.). Compared with the de León spectrum, different wavelength ranges were retained for the seven spectra reported by Polishook et al. (2023). As shown in Fig. 1, the spectra obtained during the first three nights were retained over 0.765–2.45 μm, while those from the subsequent four nights were retained over 0.7–2.45 μm. Under this definition of the blue edge, the Polishook spectra exhibit strong consistency with the de León spectrum in the visible region, indicating that the data are reliable. Since the maximum of the de León spectrum near 0.75 μm is located at 0.771 μm (de León et al. 2010), the adopted wavelength ranges for the Polishook spectra encompass this feature, ensuring that the spectral analysis is not affected.

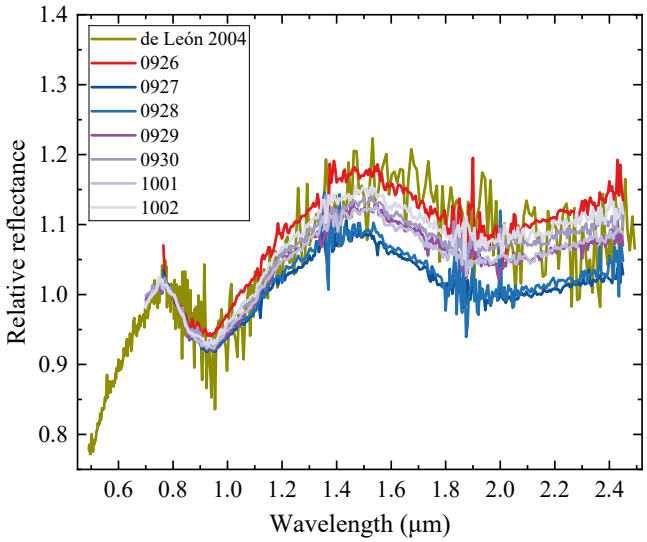

Fig. 1: Seven VNIR spectra (obtained by Polishook et al. 2023) of the Didymos system before and after the DART impact. The de León spectrum is also plotted for comparison. All spectra were normalized at 0.77 μm.

2.2. Spectra and mineralogical compositions of meteorite analogs

A dataset of 81 ordinary chondrites containing both spectral and mineralogical information was compiled. The selected ordinary chondrites were, as far as possible, chosen to have similar grain sizes and to be falls. Among them, 53 provide ol/(ol+px) values, 76 provide Fa values, and 70 provide Fs values. The dataset is approximately twice the size of that used by Dunn et al. (2010b) and was employed to derive new calibration equations. The spectra of these meteorites were obtained from the NASA RELAB database (updated December 31, 2025, Pieters & Hiroi 2004)[1], and their detailed information is recorded in Table A.1.

To distinguish the influences of space weathering and grain size on the spectra of different meteorite analogs, we compiled a meteorite dataset comprising 34 samples and 79 spectra (Table A.2). The dataset covers all petrologic types within the three ordinary chondrite subtypes (H, L, and LL). These laboratory spectra were obtained from the NASA RELAB database and the Centre for Terrestrial and Planetary Exploration (C-TAPE) collection[2] and were restricted to measurements from the same

[1] https://pds-speclib.rsl.wustl.edu/search.aspx?catalog=RELAB
[2] https://www.uwinnipeg.ca/c-tape/sample-database.html

meteorite portion at multiple particle-size bins, where spectra differ primarily by sieving to minimize composition-related effects. Except for two spectra from the C-TAPE collection for which the temperature was not recorded, all measurements were acquired at a phase angle of 30° and at room temperature.

2.3. Band parameter analysis methods

The spectra of asteroids and meteorites were denoised using cubic spline smoothing, followed by the removal of the linear continuum for the two absorption bands. For Band I, the left endpoint of the linear continuum was defined as the local maximum near 0.75 μm, and the right endpoint was defined as the tangent point obtained by drawing a tangent from the left endpoint toward the region near 1.5 μm. For Band II, the right endpoint of the linear continuum was defined as the point at 2.4 μm, and the left endpoint was defined as the tangent point obtained by drawing a tangent from the right endpoint toward the region near 1.5 μm. In this work, the right endpoint of Band II was set to 2.4 μm because, in near-Earth space, the reflectance spectra of silicate surfaces are non-negligibly affected by thermal emission beyond 2.4 μm (Wu et al. 2021). The slope of each absorption band is defined as the slope of its linear continuum, and the band width is defined as the wavelength difference between the right and left endpoints.

After continuum removal, the lower 30% of Band I and Band II were fit with a fifth-order polynomial and a sixth-order polynomial, respectively. The band center is defined as the minimum of the polynomial, and the band depth is defined as the depth at this minimum. The uncertainties of the band parameters for the asteroid spectra were estimated using a Monte Carlo approach. Specifically, Gaussian noise consistent with the measured spectral uncertainties was added to the reflectance values, and the band parameters were recalculated 10 000 times. The final parameter values correspond to the mean of these simulations, while the associated uncertainties were defined as the standard deviations of the resulting distributions. The uncertainties were estimated only for the asteroid spectra, as the meteorite spectra have sufficiently high signal-to-noise ratios.

3. Results

3.1. Calibration formulae for mineralogical parameters

Table B.1 presents the band parameters of the meteorite spectra used in this study. By correlating these parameters with the mineralogical parameters in Table A.1, a set of mineralogical calibration equations was established.

3.1.1. Calibration equation for ol/(ol + px)

Consistent with the previous study (Dunn et al. 2010b), we found that ol/(ol + px) is inversely correlated with BAR. Figure 2 shows the linear regression of ol/(ol + px) as a function of BAR, together with the calibration line reported by Dunn et al. (2010b) for comparison. The two lines are very similar; the small offset mainly reflects the different Band II red edge choices adopted in the two BPA methods, namely 2.4 μm in this work and 2.5 μm in Dunn et al. (2010b). Because using 2.4 μm yields slightly smaller BAR values, our fit line lies slightly to the left of theirs. A least-squares fit of the data yields the calibration equation for ol/(ol + px):

$$ol/(ol+px) = -0.2720 \times BAR + 0.7176, \quad (1)$$

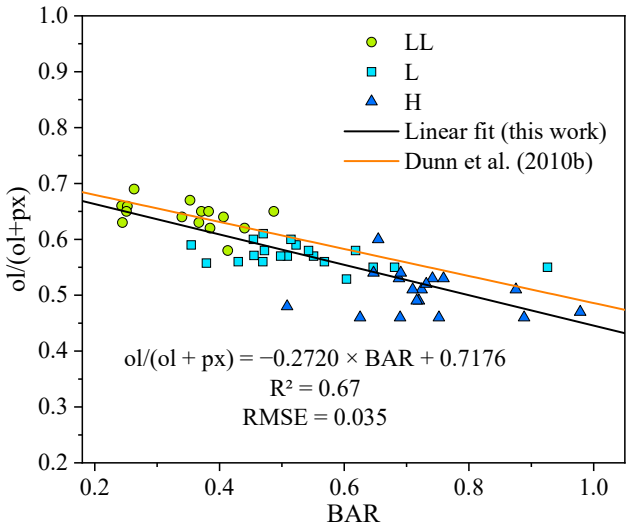

Fig. 2: Linear regression of ol/(ol + px) as a function of BAR. The linear fit derived in this work is also shown in the figure.

with an R^2 value of 0.67 and a root mean square error of the spectrally derived ol/(ol + px) ratios is 0.035.

3.1.2. Calibration equations for Fa and Fs

Different from Dunn et al. (2010b), we found that using a cubic polynomial provides a better fit for Fa and Fs as a function of BIC, which results from differences in BPA methods. It should be noted that, as in Dunn et al. (2010b), eight outlier samples were excluded from the fitting. Their names are indicated in italics in Table B.1. In addition, two samples (Apt and Dhurmsala) have Fs values that slightly exceed the range defined by Brearley & Jones (1998), and thus were not included in the fitting process.

Figure 3 shows the cubic polynomial fit of Fa and Fs as a function of BIC, together with the calibration curves reported by Dunn et al. (2010b) for comparison. The differences mainly arise because Dunn et al. (2010b) used a quadratic polynomial to determine BIC, whereas we used a quintic polynomial, which better traces the band shape; the quadratic fit tends to place the band center slightly at longer wavelengths, so our curve lies slightly to the left of theirs. A least-squares fit of the data yields the calibration equations for Fa and Fs:

$$Fa = 20650.7630 \times \mathrm{BIC}^3 - 62305.0382 \times \mathrm{BIC}^2 + 62652.1517 \times \mathrm{BIC} - 20967.4036, \quad (2)$$

$$Fs = 16244.5059\,\mathrm{BIC}^3 - 48922.5036\,\mathrm{BIC}^2 + 49102.6019\,\mathrm{BIC} - 16399.5173, \quad (3)$$

where Fa and Fs are in mol% and BIC is in μm, with R^2 values of 0.85 and 0.83 and RMSE of 1.60 and 1.26 for the spectrally derived Fa and Fs, respectively.

3.2. Spectral changes of the Didymos system during the DART impact

Following the DART impact, the contribution of Dimorphos ejecta to the Didymos system spectrum decreased from 64% in the 0927 spectrum to 23% in the 1002 spectrum.

Table 1.: Band parameters and mineralogical parameters inferred from seven spectra of the Didymos system, as well as their mean values.

Date	BIS (μm^{-1})	BIC (μm)	BAR	ol/(ol + px)	Fa (mol%)	Fs (mol%)
0926	0.1928 ± 0.0085	0.9468 ± 0.0029	0.8258 ± 0.0432	0.493	26.66	22.58
0927	0.0924 ± 0.0061	0.9408 ± 0.0013	0.7905 ± 0.0313	0.503	25.29	21.58
0928	0.1059 ± 0.0058	0.9424 ± 0.0014	0.9038 ± 0.0372	0.472	25.68	21.87
0929	0.1620 ± 0.0029	0.9445 ± 0.0014	0.6515 ± 0.0215	0.540	26.17	22.22
0930	0.1697 ± 0.0033	0.9439 ± 0.0013	0.7419 ± 0.0233	0.516	26.03	22.12
1001	0.1594 ± 0.0032	0.9429 ± 0.0015	0.7477 ± 0.0237	0.514	25.80	21.95
1002	0.1972 ± 0.0041	0.9384 ± 0.0017	0.7361 ± 0.0289	0.517	24.65	21.12
Average[a]	–	–	–	0.508 ± 0.022	25.76 ± 0.65	21.92 ± 0.47

Notes. [(a)]For the mineralogical parameters in the "Average" row, the quoted uncertainties ($\pm 1\sigma$) are the standard deviations of the seven individual estimates derived from the seven spectra.

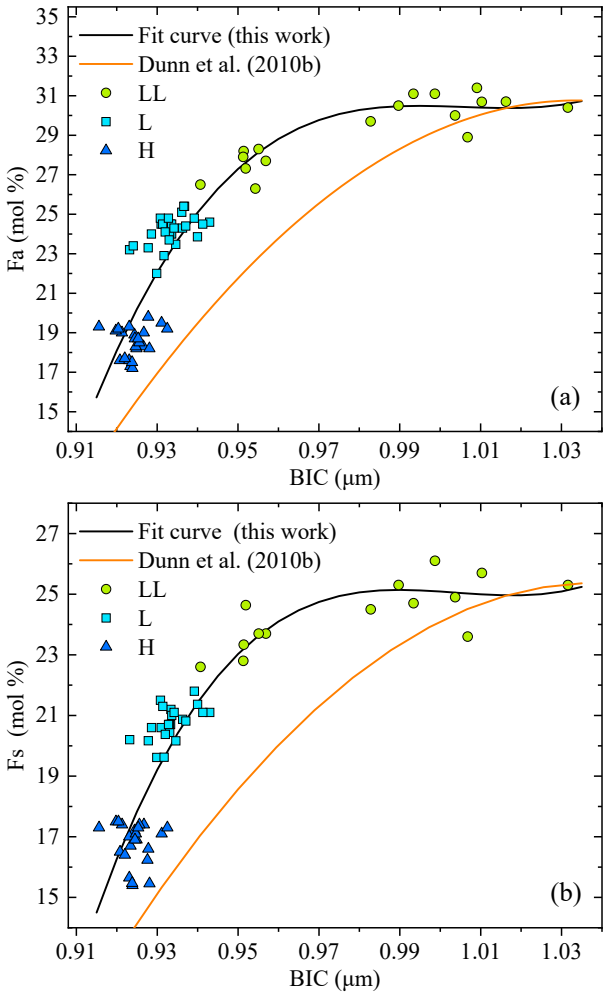

Fig. 3: Cubic polynomial regression of BIC vs. Fa and Fs.

Polishook et al. (2023) reported that the system's spectral slopes, derived from linear fits to the reflectance spectrum over 0.8–2.45 μm and 0.8–1.5 μm, decreased during the first two post-impact days and then gradually returned to the pre-impact level over the following nights. Here we obtained the linear continuum slope of Band I (BIS), computed between the left endpoint and the right endpoint of Band I, for the same seven spectra, and found the same temporal evolution: BIS decreases during the first two post-impact days and subsequently recovers toward the pre-impact value (Table 1; Fig. 1). This behavior may result from differences in the degree of space weathering and/or grain size between the ejecta from Dimorphos and the surface of Didymos.

The ratio spectrum, i.e., the ratio of one spectrum to another, is an effective method of investigating spectral differences (Gaffey & Gilbert 1998; Brunetto et al. 2006; Mahlke et al. 2023). Experimental studies simulating solar wind irradiation indicate that solar-wind-induced space weathering primarily affects the continuum of the spectrum, while exerting negligible influence on absorption features (Brunetto et al. 2006; Strazzulla et al. 2005; Brunetto & Strazzulla 2005). Dividing the weathered spectrum by the unweathered spectrum yields a ratio spectrum that exhibits a convex upward shape. This curve can be well described by the following equation (Brunetto et al. 2006):

$$W(\lambda) = K \exp\left(\frac{C_S}{\lambda}\right), \tag{4}$$

where $W(\lambda)$ is the weathering function, i.e., the ratio between the weathered and unweathered spectra, λ is the wavelength, and K is a scaling factor that varies with spectral normalization. The parameter C_S is negative, representing the curvature of the exponential function, and serves as an indicator of the degree of weathering. A larger absolute value of C_S corresponds to a stronger curvature of the weathering function, indicating a higher degree of weathering. Brunetto et al. (2006) noted that the model works well over 0.3–2.0 μm, whereas in the 2.0–2.5 μm region the fit becomes less accurate, with deviations typically smaller than about 5%.

Few studies have investigated grain size effect using ratio spectra, and it is challenging to distinguish space weathering effect and grain size effect from spectra. In this section, we attempt to use ratio spectra to distinguish space weathering effect and grain size effect, and apply these findings to interpret the spectral variations in the Didymos system.

3.2.1. The ratio spectra of the Didymos system

Figure 4 shows the ratio spectra of the other six spectra with respect to the 0927 spectrum. If these spectral variations are entirely caused by space weathering, then according to Eq. (4), these ratio spectra can be expressed as

$$\frac{R_a(\lambda)}{R_{0927}(\lambda)} = \frac{W_a(\lambda)}{W_{0927}(\lambda)} = \frac{K_a}{K_{0927}} \exp\left(\frac{C_{S\,a} - C_{S\,0927}}{\lambda}\right), \tag{5}$$

where a denotes one of the other six spectra.

Figure 4 presents the results of least-squares fitting of the six ratio spectra using Eq. (5). The ratio spectra are well fit by

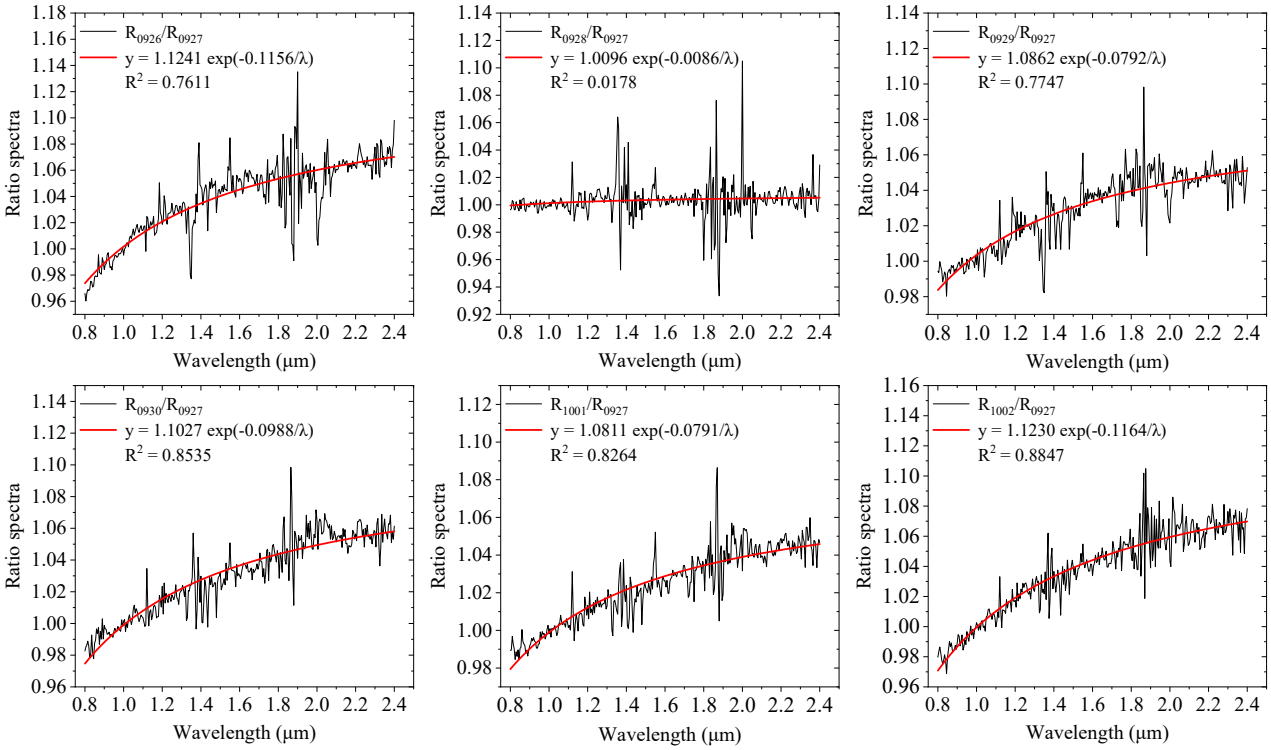

Fig. 4: Ratio spectra of the other six Didymos system spectra relative to 0927 spectrum.

Eq. (5), and no distinct 1 μm or 2 μm absorption features are observed.

However, the grain size effect can also produce similar shapes in the ratio spectra. Space weathering causes asteroid spectra to become redder and darker, whereas smaller grain sizes may make them redder and brighter (Brunetto et al. 2006; MacLennan et al. 2024). Therefore, it is difficult to distinguish between these two effects based solely on spectral slope, and a further discussion is provided in the next section.

3.2.2. The ratio spectra of the meteorite samples

By dividing the spectrum of the smaller grain size fraction by that of the larger grain size fraction, ratio spectra were obtained and fit using Eq. (5) (Fig. 5). To facilitate a comparison with the spectra of the Didymos system, the range of these ratio spectra is restricted to 0.7–2.4 μm. The $C_{S_a} - C_{S_{0927}}$ values derived from Eq. (5) are labeled beside each ratio spectrum.

As shown in Figs. 5a and b, the spectral variations caused by the grain size effect in H and L chondrites cannot be described by Eq. (5). Most samples exhibit similar behaviors over the 0.7–2.4 μm range: these ratio spectra lie above the fitting curve near 1 μm and 2 μm, which are denoted as "peaks" in this study, but fall below the fitting curve between 1 and 2 μm. This behavior may result from the fact that the spectra with larger grain sizes, used as the denominator, exhibit deeper absorption bands near 1 μm and 2 μm. In a few cases, a pronounced peak near 1 μm can yield positive fit C_S values.

This characteristic behavior is consistent with the grain-size trends reported by MacLennan et al. (2024). MacLennan et al. (2024) reported a clear grain-size dependence of the BIS: the smallest grain-size bin exhibits the largest (reddest) slopes, and the BIS distributions generally shift toward lower (bluer) values for coarser size bins (see their Fig. 2a). Their Fig. 2b further indicates that within powdered samples, larger grain sizes tend to exhibit deeper Band I absorptions. They also noted that BIS is sensitive to space weathering; therefore, BIS-based indices can complicate interpretations when grain-size variations and space weathering are both relevant.

In our ratio-spectral analysis restricted to 0.7–2.4 μm, the fit slope may be influenced by absorption band depth variations; however, when a larger-grain spectrum is used as the denominator, deeper absorptions in the denominator naturally generate the two prominent peaks near 1 and 2 μm. Therefore, this peak-bearing ratio-spectral morphology provides an additional indicator beyond a single BIS parameter for distinguishing grain size effects from space weathering in H and L chondrites (Fig. 5).

In contrast, for LL chondrites, the grain size effect is more complex. As is shown in Fig. 5c, approximately one third of the ratio spectra of LL chondrites do not exhibit the two peaks mentioned above. Moreover, despite some deviations, the fitting using Eq. (5) still performs well for these spectra. This indicates that, for LL chondrites, it is difficult to distinguish between grain size effect and space weathering effect based solely on the ratio spectra.

Therefore, identifying the specific meteoritic analog subtype is crucial for understanding the spectral variations in the Didymos system and the surfaces of other ordinary chondrite-like asteroids. For H and L chondrites, ratio spectra can help assess whether the slope variations in the asteroid system or surface are primarily dominated by grain size effect or by space weathering. However, for LL chondrites, the situation is more complex and warrants further investigation in future studies. We believe that this method of distinction should also be applicable to some other meteorite analogs that exhibit spectral absorption features, which is worth investigating in the future.

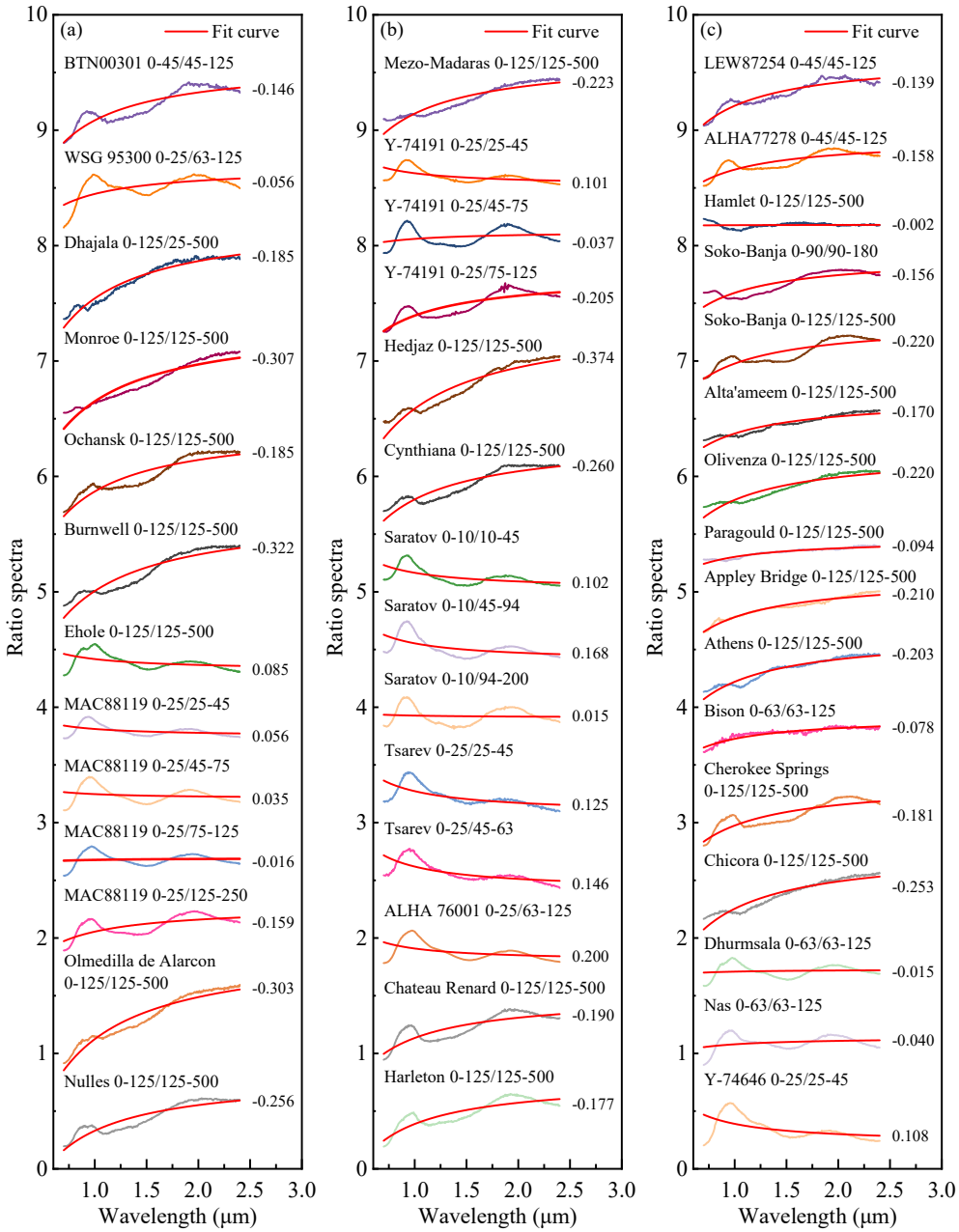

Fig. 5: Ratio spectra of ordinary chondrites with different grain sizes, obtained by dividing the spectrum of the smaller grain size fraction by that of the larger grain size fraction, and fit using the weathering function defined by Eq. (5). (a) Thirteen ratio spectra of H chondrites from 10 meteorites; (b) fourteen ratio spectra of L chondrites from 9 meteorites; (c) sixteen ratio spectra of LL chondrites from 15 meteorites. For clearer visualization, the spectra are appropriately scaled and vertically offset. The $C_{S_a} - C_{S_{0927}}$ values derived from Eq. (5) are labeled beside each ratio spectrum. The poor fit indicates that the weathering function is not suitable for describing grain size effects.

3.3. Meteorite analog and mineral composition of Didymos

The reddening of spectra is the main cause of the mismatch between asteroid spectra and meteorites in band parameters. To obtain accurate spectral parameters, the spectra of Didymos were de-reddened using Eq. (4) so that their Band I continuum slopes matched the average slope (0.029 μm^{-1}) calculated from ordinary chondrite spectra that were normalized at 0.55 μm. The band parameters (BIS, BIC, and BAR, with their associated uncertainties) were computed from the Didymos spectra, with BIS measured on the original spectra to quantify reddening, BIC and BAR measured on the de-reddened spectra; BIC and BAR were then used in Eqs. (1–3) to derive the corresponding mineralogical parameters, as summarized in Table 1. The derived BIC and BAR values are in good agreement with those reported by Polishook et al. (2023); the small differences reflect methodological variations among different BPA methods, underscoring the importance of using self-consistent calibration relations.

Figure 6 shows the projections of seven spectra of the Didymos system in the Fa vs. ol/(ol + px) and Fs vs. ol/(ol + px) plots, along with their average values. Error bars represent the

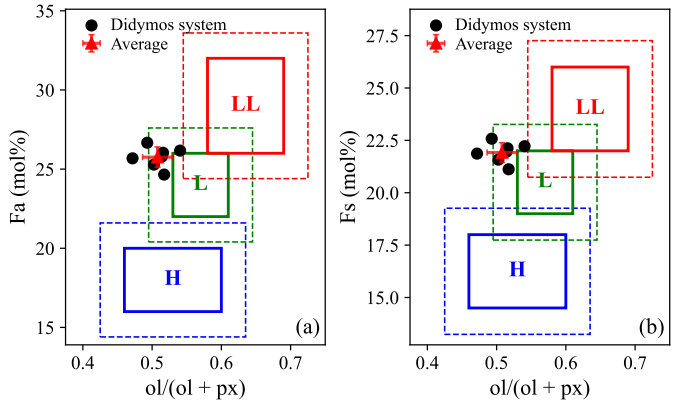

Fig. 6: Projection of mineralogical parameters derived from seven spectra of the Didymos system. (a) Projection in the Fa vs. ol/(ol + px) space. (b) Projection in the Fs vs. ol/(ol + px) space. The mean values of these parameters are also shown, with error bars representing the standard deviations of the seven individual estimates derived from the seven spectra. The solid-line boxes in the figure represent the ranges of measured mineralogical parameters for the three subtypes (Brearley & Jones 1998; Dunn et al. 2010b), while the dashed-line boxes denote the ranges considering the RMSE values given by the calibration equations, with RMSEs of 0.035 for ol/(ol + px), 1.60 for Fa, and 1.26 for Fs.

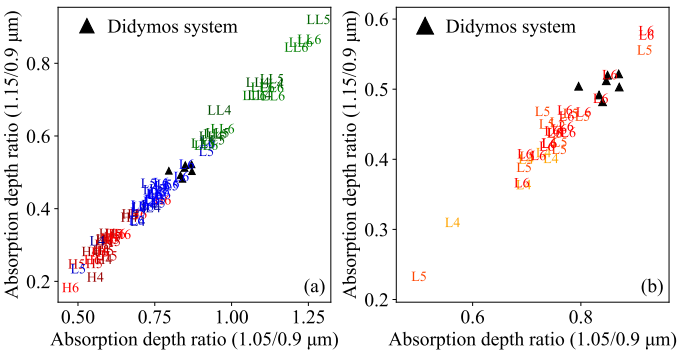

Fig. 7: Absorption depth ratios at 1.05 and 1.15 μm relative to 0.9 μm of the Didymos spectra. (a) Comparison with H (red), L (blue), and LL (green) chondrites. (b) Detailed comparison with L chondrites, where L6, L5, and L4 are shown in red, orange, and yellow, respectively, indicating increasing degrees of thermal metamorphism.

quoted uncertainties, defined as the standard deviations of the seven individual estimates derived from the seven spectra. The solid-line boxes in the figure represent the ranges of measured mineralogical parameters for the three subtypes, as reported by Brearley & Jones (1998) and Dunn et al. (2010b), while the dashed-line boxes denote the ranges considering the RMSE values given by the calibration equations, with RMSEs of 0.035 for ol/(ol + px), 1.60 for Fa, and 1.26 for Fs. The mineralogical ranges of these seven spectra are highly concentrated and largely fall within the L chondrite field; although the uncertainties allow some overlap with the LL field in Fa and Fs, the ol/(ol + px) constraint keeps Didymos outside the LL region, so an L chondrite analog is favored, while an LL subtype cannot be strictly ruled out.

By comparing the absorption depth ratios in the near-infrared spectra, Abe et al. (2006) successfully predicted the meteorite analog and petrologic type of Itokawa. In this study, we adopted their definition of band parameters, calculated the absorption depth ratios at 1.05 μm and 1.15 μm relative to 0.9 μm for meteorites, and projected the Didymos spectra onto the plot (Fig. 7). The three types of ordinary chondrites are clearly distinguishable in Fig. 7a, with only a few overlaps. The Didymos spectra are located within the L chondrite region and close to the boundary with the LL field, consistent with the results shown in Fig. 6. However, unlike Abe et al. (2006), when additional meteorite sample data are included, the petrologic types are less distinctly separated, although the overall trend remains the same as in Fig. 4 of Abe et al. (2006), with petrologic types increasing toward the upper right. For a more detailed comparison, Fig. 7b shows only L chondrites and the Didymos system. In this plot, Didymos occupies the upper right region of the L chondrite field, where it is surrounded by six L6 data points and one L5 data point. The L5 point appears to be an outlier and lies close to the boundary with the LL field. Therefore, the available data suggest that Didymos is most consistent with highly metamorphosed L chondrites, most similar to L6, although a type 5 interpretation cannot be entirely excluded.

4. Discussion

4.1. The causes of spectral variations in the Didymos system

Section 3.2 indicates that the spectral changes in the Didymos system can be well described by Eq. (5). However, the interpretation of asteroid spectral variations depends on its meteorite analog. Section 3.3 indicates that the meteorite analog of the Didymos system is most consistent with L ordinary chondrites, with a minor possibility of LL, suggesting that the ratio spectra can help distinguish between the effects of space weathering and grain size on Didymos. If the spectral changes of the Didymos system were dominated by space weathering, its ratio spectra would be expected to be well described by Eq. (5), and no peaks would appear at 1 μm and 2 μm. In contrast, such features are not observed in Fig. 4. Therefore, the spectral changes of Didymos are more likely dominated by space weathering, although minor contributions from grain size effects cannot be entirely excluded.

4.2. Formation of the Didymos binary system

The mineral compositions derived from the seven spectra of the Didymos system are highly similar (Sect. 3.3), and the spectral variations are primarily caused by space weathering rather than grain size effect or compositional differences (Sect. 4.1), indicating that Didymos and Dimorphos are compositionally homogeneous, consistent with the hypothesis that the Didymos system formed via rotational fission (Pajola et al. 2024; Barnouin et al. 2024).

Further support comes from the surface exposure age of Didymos. Rotational fission is an effective mechanism for refreshing asteroid surfaces (DeMeo et al. 2023). If Dimorphos originated from material ejected from Didymos, the surface exposure age of Didymos and the surface crater retention age of Dimorphos should be consistent. The C_S value was originally introduced to characterize the degree of space weathering and is linked to the exposure age of asteroids (Brunetto et al. 2006). Given that the spectral variations in the Didymos system are primarily governed by space weathering, the exposure age of Didymos can likewise be inferred from the C_S value of the 0926 spectrum. Applying the method of Brunetto et al. (2006), the exposure age of Didymos was estimated to be ~0.39 Myr

(see Appendix C for details of the calculation). Recent studies indicate that the surface crater retention age on Dimorphos is 0.09–0.3 Myr (Barnouin et al. 2024), which is consistent with the exposure age derived in this work. This provides new evidence supporting the hypothesis that Didymos formed through rotational fission. The derived exposure age constrains the timing of the major mass-shedding event experienced by Didymos to approximately 0.39 Myr ago.

4.3. Meteorite analog and origin of Didymos system

The meteorite analog of the Didymos system is most consistent with L ordinary chondrites, and the derived band parameters suggest a highly metamorphosed petrologic type, most similar to L6. According to the onion-shell model, regions closer to the center of the L chondrite parent body experienced higher degrees of thermal metamorphism, corresponding to higher petrologic types (Gail & Trieloff 2019). This suggests that the Didymos system originated from the highly thermally metamorphosed inner regions of an L chondrite parent body.

5. Conclusions

Based on the analyses conducted in this study, we characterized the spectral changes of the Didymos system and identified the corresponding meteorite analogs, which are essential for interpreting these variations. By compiling an extensive dataset of meteorite spectra along with their mineralogical parameters, we derived new calibration equations that were applied to determine the mineralogical compositions of the Didymos system. The following conclusions are drawn from this study:

(1) The meteorite analog of Didymos is most consistent with L ordinary chondrites. The derived band parameters further suggest a highly metamorphosed petrologic type, most similar to L6, although type 5 cannot be entirely excluded, indicating that Didymos experienced extensive thermal metamorphism and suggesting that the Didymos system originated from the highly thermally metamorphosed inner regions of the L chondrite parent body;

(2) For H and L chondrites, ratio spectra can help assess whether the slope variations in the asteroid system or surface are primarily dominated by the grain size effect. However, for LL chondrites, the situation is more complex, as these two effects cannot be easily distinguished. Based on the ratio spectra of the Didymos system, it can be concluded that the spectral changes of Didymos are primarily dominated by space weathering rather than by grain size effect or compositional differences;

(3) The surface of Didymos has an exposure age of ~0.39 Myr, which is consistent with the recently reported surface crater retention age on Dimorphos. This suggests that ~0.39 Myr ago the primary may have undergone a large-scale mass-shedding event that simultaneously reset the surface crater retention age of Dimorphos and the exposure age of Didymos, providing new evidence supporting the rotational fission mechanism as the formation process of the Didymos system.

These results provide useful insights into the origin and evolution of the Didymos system and contribute to understanding the effects of the DART impact.

Acknowledgements. This research was supported by the Macau Science and Technology Development Fund (0094/2024/RIA2), the Natural Science Foundation of Jiangsu Province (BK20252110), National Natural Science Foundation of China (12150009) and the Foundation of Minor Planets of the Purple Mountain Observatory. We thank David Polishook (Weizmann Institute of Science) for kindly providing the near-infrared spectral data of the Didymos system. This research utilizes spectra acquired by various investigators with the NASA RELAB facility at Brown University. We thank Edward Cloutis for providing laboratory spectra from the C-TAPE collection and for helpful assistance with the dataset, and we acknowledge C-TAPE at the University of Winnipeg for access to laboratory spectral data.

References

Abe, M., Takagi, Y., Kitazato, K., et al. 2006, Science, 312, 1334
Adams, J. B. 1974, J. Geophys. Res., 79, 4829
Barnouin, O., Ballouz, R.-L., Marchi, S., et al. 2024, Nat. Commun., 15, 6202
Brearley, A. J., & Jones, R. H. 1998, Rev. Mineral. Geochem., 36, 3
Brunetto, R., & Strazzulla, G. 2005, Icarus, 179, 265
Brunetto, R., Vernazza, P., Marchi, S., et al. 2006, Icarus, 184, 327
Burbine, T. H., McCoy, T. J., Jarosewich, E., & Sunshine, J. M. 2003, Antarct. Meteorite Res., 16, 185
Burns, R. G. 1970, Am. Mineral., 55, 1608
Burns, R. G., Huggins, F. E., & Abu-Eid, R. M. 1972, Moon, 4, 93
Cloutis, E. A. 1985, Master's thesis, University of Hawai'i at Manoa
Cloutis, E. A., Gaffey, M. J., Jackowski, T. L., & Reed, K. L. 1986, J. Geophys. Res., 91, 11641
de León, J., Licandro, J., Duffard, R., & Serra-Ricart, M. 2006, Adv. Space Res., 37, 178
de León, J. d., Licandro, J., Serra-Ricart, M., Pinilla-Alonso, N., & Campins, H. 2010, A&A, 517, A23
DeMeo, F. E., Marsset, M., Polishook, D., et al. 2023, Icarus, 389, 115264
Dunn, T. L., Cressey, G., McSWeen Jr, H. Y., & McCOY, T. J. 2010a, Meteorit. Planet. Sci., 45, 123
Dunn, T. L., McCoy, T. J., Sunshine, J. M., & McSween, H. Y. 2010b, Icarus, 208, 789
Dunn, T. L., McSween Jr, H. Y., McCOY, T. J., & Cressey, G. 2010c, Meteorit. Planet. Sci., 45, 135
Dunn, T. L., Burbine, T. H., Bottke, W. F., & Clark, J. P. 2013, Icarus, 222, 273
Gaffey, M. J., & Gilbert, S. L. 1998, Meteorit. Planet. Sci., 33, 1281
Gaffey, M., Cloutis, E., Kelley, M., & Reed, K. 2002, Mineralogy of Asteroids (University of Arizona Press), 183
Gail, H.-P., & Trieloff, M. 2019, A&A, 628, A77
Gomes, C. B., & Keil, K. 1980, Brazilian stone meteorites: with a brief, general introduction on the significance, classification, mineralogy, bulk composition, and recognition of stone meteorites (Albuquerque: University of New Mexico Press)
Heyse, J. V. 1978, Earth Planet. Sci. Lett., 40, 365
Ieva, S., Epifani, E. M., Perna, D., et al. 2022, Planet. Sci. J., 3, 183
Ieva, S., Epifani, E. M., Dotto, E., et al. 2024, Planet. Sci. J., 5, 225
Keil, K., & Fredriksson, K. 1964, J. Geophys. Res., 69, 3487
King, T. V. V., & Ridley, W. I. 1987, J. Geophys. Res.: Solid Earth, 92, 11457
Korda, D., Penttila, A., Klami, A., & Kohout, T. 2023, A&A, 669, A101
Lindsay, S. S., Dunn, T. L., Emery, J. P., & Bowles, N. E. 2016, Meteorit. Planet. Sci., 51, 806
MacLennan, E. M., Emery, J. P., Lucas, M. P., McClure, L. M., & Lindsay, S. S. 2024, Meteorit. Planet. Sci., 59, 1329
Mahlke, M., Eschrig, J., Carry, B., Bonal, L., & Beck, P. 2023, A&A, 676, A94
McClure, L. T., & Lindsay, S. S. 2022, Icarus, 379, 114907
Mitchell, A. M., Reddy, V., Sharkey, B. N. L., et al. 2020, Icarus, 336, 113426
Oshtrakh, M. I., Maksimova, A. A., Chukin, A. V., et al. 2019, Spectrochim. Acta A, 219, 206
Pajola, M., Tusberti, F., Lucchetti, A., et al. 2024, Nat. Commun., 15, 6205
Pieters, C. M., & Hiroi, T. 2004, in Lunar and Planetary Science Conference, 1720
Polishook, D., DeMeo, F. E., Burt, B. J., et al. 2023, Planet. Sci. J., 4, 229
Rayner, J. T., Toomey, D. W., Onaka, P. M., et al. 2003, Publ. Astron. Soc. Pac., 115, 362
Reddy, V., Dunn, T. L., Thomas, C. A., Moskovitz, N. A., & Burbine, T. H. 2015, Mineralogy and Surface Composition of Asteroids (University of Arizona Press)
Rivkin, A. S., Thomas, C. A., Wong, I., et al. 2023, Planet. Sci. J., 4, 214
Rubin, A. E. 1990, Geochim. Cosmochim. Acta, 54, 1217
Sanchez, J. A., Thomas, C., Reddy, V., et al. 2020, Astron. J., 159, 146
Strazzulla, G., Dotto, E., Binzel, R., et al. 2005, Icarus, 174, 31
Weisberg, M. K., McCoy, T. J., & Krot, A. N. 2006, in Meteorites and the Early Solar System II (University of Arizona Press)
Wu, Y., Li, L., Luo, X., et al. 2018, Icarus, 303, 67
Wu, Y., Kührt, E., Grott, M., et al. 2021, Geophys. Res. Lett., 48, e2020GL089226

Appendix A: Meteorite information

Table A.1: Meteorites used in this study and their mineralogical information.

Type	Sample name	RELAB ID	Grain size	ol/(ol + px)[a]	Fa[a,b]	Fs[a,b]	References[c]
H4	Avanhandava	TB-TJM-066	<150 μm	-	17.3	16.7	a
H4	Conquista	TB-MDD-297	<10 μm	-	17.2	15.4	a
H4	Farmville	TB-TJM-128	<150 μm	0.46	17.6	16.5	b,c
H4	Forest Vale	TB-TJM-093	<75 μm	0.48	18.3	-	b,d
H4	Kabo	TB-TJM-136	<150 μm	0.46	18.2	16.9	b,c
H4	Marilia	TB-TJM-078	<150 μm	0.46	-	-	b
H4	Monroe	OC-TXH-005-C	<125 μm	-	17.6	15.6	e
H4	Ochansk	OC-TXH-008-C	<125 μm	-	17.5	15.5	e
H4	São Jose do Rio Preto	TB-TJM-082	<150 μm	0.46	18.9	17.2	b,c
H5	Allegan	TB-TJM-104	nm[d]	0.47	17.7	16.4	b,c
H5	Ehole	TB-TJM-074	<150 μm	0.51	19.3	17.0	b,c
H5	Itapicuru-Mirim	TB-TJM-097	<150 μm	0.53	18.3	17.1	b,c
H5	Lost City	TB-TJM-129	<150 μm	0.49	18.7	16.9	b,c
H5	Macau	TB-MDD-326	<10 μm	-	19.0	17.4	a
H5	Pribram	TB-TJM-143	<150 μm	0.49	18.5	17.4	b,c
H5	Pultusk	MH-CMP-009-B	<250μm	-	18.2	15.5	e
H5	Schenectady	TB-TJM-083	<150 μm	0.54	19.0	17.4	b,c
H5	Uberaba	TB-TJM-085	<150 μm	0.51	19.5	17.1	b,f
H6	Andura	TB-TJM-088	<75 μm	0.53	19.3	17.3	b,c
H6	Butsura	TB-TJM-069	<150 μm	0.51	19.1	17.5	b,c
H6	Canon City	TB-TJM-131	<150 μm	0.54	19.2	17.3	b,c
H6	Chiang Khan	TB-TJM-132	<150 μm	0.53	19.8	16.6	b,g
H6	Guarena	TB-TJM-094	<150 μm	0.60	19.2	17.5	b,c
H6	Ipiranga	TB-TJM-135	<150 μm	0.52	18.7	17.3	b,c
H6	Kernouve	DP-JNG-013	<125 μm	-	-	16.2	e
H6	Portales Valley	MT-DTB-057	<250 μm	-	19.6	17.2	g
L4	Atarra	TB-TJM-065	<150 μm	0.56	23.2	20.2	b,c
L4	Bald Mountain	TB-TJM-102	<150 μm	0.55	22.9	19.9	b,c
L4	Barratta	MH-CMP-002	<250 μm	-	23.4	-	d
L4	Rio Negro	TB-TJM-081	<150 μm	0.55	24.5	20.6	b,c
L4	Rupota	TB-TJM-121	<150 μm	0.57	24.5	20.7	b,c
L5	Ausson	MT-HYM-084	<150 μm	0.55	24.7	21.3	b,c
L5	Blackwell	MT-HYM-081	<150 μm	0.56	-	-	b
L5	Cilimus	MT-HYM-082	<150 μm	0.58	24.0	20.6	b,g
L5	Elenovka	MS-CMP-041-A	<75 μm	-	25.4	-	d
L5	Ergheo	MH-CMP-021	<250 μm	-	23.7	20.3	e
L5	Guibga	TB-TJM-134	<150 μm	0.58	24.1	21.2	b,c
L5	Homestead	TB-MDD-309	<10 μm	-	22.0	19.6	e
L5	Mabwe-Khoywa	TB-TJM-107	<150 μm	0.58	-	-	b
L5	Malakal	TB-TJM-109	<150 μm	0.57	24.8	21.5	b,c
L5	Messina	TB-TJM-099	<150 μm	0.57	24.5	21.3	b,c
L5	Shelburne	TB-TJM-122	<150 μm	-	24.0	-	d
L5	Tsarev	RS-CMP-047-P4	<63 μm	0.53	23.9	21.4	g
L6	Air	TB-TJM-063	<150 μm	-	23.5	20.2	g
L6	Apt	TB-TJM-064	<150 μm	0.56	25.1	22.2	b,c
L6	Aumale	TB-TJM-101	<150 μm	0.59	24.5	21.0	b,c
L6	Bath Furnace	TB-MDD-287	<10 μm	-	24.0	20.4	e
L6	Chantonnay	TB-TJM-070	<150 μm	-	23.3	20.2	e
L6	Chateau Renard	OC-TXH-011-C	<125 μm	0.56	23.7	20.2	e,g
L6	Denver	TB-TJM-072	<150 μm	-	25.4	-	d
L6	Girgenti	TB-TJM-103	<150 μm	0.57	24.3	20.9	e,g
L6	Harleton	OC-TXH-003-C	<125 μm	-	24.1	20.4	e
L6	Karkh	TB-TJM-137	<150 μm	0.59	24.8	21.8	b,c
L6	Kunashak	TB-TJM-139	<150 μm	0.60	24.6	21.1	b,c
L6	Kuttippuram	TB-TJM-098	<75 μm	-	24.1	20.4	e
L6	Kyushu	TB-TJM-140	<150 μm	0.61	24.5	21.1	b,c
L6	L'Aigle	TB-TJM-141	<150 μm	-	22.9	19.6	e

Table A.1: continued.

Type	Sample name	RELAB ID	Grain size	ol/(ol + px) [a]	Fa [a,b]	Fs [a,b]	References [c]
L6	New Concord	TB-TJM-130	<150 µm	0.60	24.3	21.1	b,c
L6	Paranaiba	TB-TJM-142	<75 µm	-	23.7	20.7	a
L6	Patrimonio	TB-TJM-113	<150 µm	-	24.8	20.7	a
L6	Walters	MP-DTB-029-A	<250 µm	-	24.4	20.8	e
LL4	Benares(a)	MT-HYM-083	<150 µm	0.58	28.9	23.6	b,c
LL4	Greenwell Springs	TB-TJM-075	<150 µm	0.64	28.2	23.3	b,g
LL4	Hamlet	MT-HYM-075	<150 µm	0.62	26.5	22.6	b,c
LL4	Soko-Banja	OC-TXH-017-C	<125 µm	-	26.9	22.5	e
LL4	Witsand Farm	MT-HYM-076	<150 µm	0.65	-	-	b
LL5	Aldsworth	MT-HYM-077	<150 µm	0.65	28.2	23.6	b,c
LL5	Alta'ameem	MT-HYM-078	<150 µm	0.62	27.3	24.6	b,g
LL5	Chelyabinsk	MT-LAT-229	<125 µm	0.63	27.9	22.8	h
LL5	Olivenza	MT-HYM-085	<150 µm	0.64	30.0	24.9	b,c
LL5	Paragould	MT-HYM-079	<150 µm	0.65	27.7	23.7	b,c
LL5	Tuxtuac	MT-HYM-080	<150 µm	0.63	30.4	25.3	b,c
LL6	Appley Bridge	OC-TXH-012-C	<125 µm	-	31.4	-	d
LL6	Athens	OC-TXH-013-C	<125 µm	-	30.7	-	d
LL6	Bandong	TB-TJM-067	<150 µm	0.66	30.5	25.3	b,c
LL6	Bensour	OC-SXS-022-D	<250 µm	0.66	31.1	24.7	g
LL6	Cherokee Springs	TB-TJM-090	<150 µm	0.67	28.3	23.7	b,c
LL6	Chicora	OC-TXH-014-C	<125 µm	-	30.7	25.7	i
LL6	Dhurmsala	MB-TXH-090-B	<125 µm	-	26.3	21.8	e
LL6	Karatu	TB-TJM-077	<75 µm	0.69	31.1	26.1	b,c
LL6	Saint Séverin	TB-TJM-145	<150 µm	0.65	29.7	24.5	b,c

Notes. [a]"–" symbol indicates missing data. [b]The units of Fa and Fs are mol%. [c]References: [a]Gomes & Keil (1980); [b]Dunn et al. (2010a); [c]Dunn et al. (2010c); [d]Rubin (1990); [e]Keil & Fredriksson (1964); [f]Brearley & Jones (1998); [g]Korda et al. (2023); [h]Oshtrakh et al. (2019); [i]Heyse (1978); [d]"nm" indicates that no sieved grain-size fraction was provided (i.e., none measured / not sieved; Burbine et al. 2003).

Table A.2: Meteorite spectra with varying grain sizes.

Type	Sample name	Spectrum ID	Grain size
H3.3	BTN00301,7	MT-PFV-167-A	0-45 µm
H3.3	BTN00301,7	MT-PFV-167-B	45-125 µm
H3.3	WSG 95300,113	MT-MDL-367-A	0-25 µm
H3.3	WSG 95300,113	MT-MDL-367-B	63-125 µm
H3.8	Dhajala	OC-TXH-020-C	0-125 µm
H3.8	Dhajala	OC-TXH-020-B	125-500 µm
H4	Monroe	OC-TXH-005-C	0-125 µm
H4	Monroe	OC-TXH-005-B	125-500 µm
H4	Ochansk	OC-TXH-008-C	0-125 µm
H4	Ochansk	OC-TXH-008-B	125-500 µm
H4-anomalous	Burnwell	OC-TXH-021-C	0-125 µm
H4-anomalous	Burnwell	OC-TXH-021-B	125-500 µm
H5	Ehole	OC-TXH-006-C	0-125 µm
H5	Ehole	OC-TXH-006-B	125-500 µm
H5	MAC 88119,9	MB-TXH-044-A	0-25 µm
H5	MAC 88119,9	MB-TXH-044-B	25-45 µm
H5	MAC 88119,9	MB-TXH-044-C	45-75 µm
H5	MAC 88119,9	MB-TXH-044-D	75-125 µm
H5	MAC 88119,9	MB-TXH-044-E	125-250 µm
H5	Olmedilla de Alarcon	OC-TXH-019-C	0-125 µm
H5	Olmedilla de Alarcon	OC-TXH-019-B	125-500 µm
H6	Nulles	OC-TXH-018-C	0-125 µm
H6	Nulles	OC-TXH-018-B	125-500 µm
L3.7	Mezo-Madaras	OC-TXH-004-C	0-125 µm
L3.7	Mezo-Madaras	OC-TXH-004-B	125-500 µm
L3.7	Y-74191	MB-TXH-084-A	0-25 µm
L3.7	Y-74191	MB-TXH-084-B	25-45 µm
L3.7	Y-74191	MB-TXH-084-C	45-75 µm

Table A.2: continued.

Type	Sample name	Spectrum ID	Grain size
L3.7	Y-74191	MB-TXH-084-D	75-125 μm
L3.7-6 breccia	Hedjaz	OC-TXH-016-C	0-125 μm
L3.7-6 breccia	Hedjaz	OC-TXH-016-B	125-500 μm
L4	Cynthiana	OC-TXH-015-C	0-125 μm
L4	Cynthiana	OC-TXH-015-B	125-500 μm
L4	Saratov	MB-CMP-028-A	0-10 μm
L4	Saratov	MB-CMP-028-B	10-45 μm
L4	Saratov	MB-CMP-028-C	45-94 μm
L4	Saratov	MB-CMP-028-D	94-200 μm
L5	Tsarev	RS-CMP-047-P8	0-25 μm
L5	Tsarev	RS-CMP-047-P9	25-45 μm
L5	Tsarev	RS-CMP-047-P10	45-63 μm
L6	ALHA 76001,35,39	MT-MDL-358-A	0-25 μm
L6	ALHA 76001,35,39	MT-MDL-358-B	63-125 μm
L6	Chateau Renard	OC-TXH-011-C	0-125 μm
L6	Chateau Renard	OC-TXH-011-B	125-500 μm
L6	Harleton	OC-TXH-003-C	0-125 μm
L6	Harleton	OC-TXH-003-B	125-500 μm
LL3.5	LEW87254,16	MT-PFV-173-A	0-45 μm
LL3.5	LEW87254,16	MT-PFV-173-B	45-125 μm
LL3.7	ALHA77278,111	MT-PFV-156-A	0-45 μm
LL3.7	ALHA77278,111	MT-PFV-156-B	45-125 μm
LL4	Hamlet	OC-TXH-002-C	0-125 μm
LL4	Hamlet	OC-TXH-002-B	125-500 μm
LL4	Soko-Banja	OC-TXH-017-C	0-125 μm
LL4	Soko-Banja	OC-TXH-017-B	125-500 μm
LL4	Soko-Banja	MJG 210[a]	0-90 μm
LL4	Soko-Banja	MJG 203[a]	90-180 μm
LL5	Alta'ameem	OC-TXH-010-C	0-125 μm
LL5	Alta'ameem	OC-TXH-010-B	125-500 μm
LL5	Olivenza	OC-TXH-009-C	0-125 μm
LL5	Olivenza	OC-TXH-009-B	125-500 μm
LL5	Paragould	OC-TXH-007-C	0-125 μm
LL5	Paragould	OC-TXH-007-B	125-500 μm
LL6	Appley Bridge	OC-TXH-012-C	0-125 μm
LL6	Appley Bridge	OC-TXH-012-B	125-500 μm
LL6	Athens	OC-TXH-013-C	0-125 μm
LL6	Athens	OC-TXH-013-B	125-500 μm
LL6	Cherokee Springs	OC-TXH-001-C	0-125 μm
LL6	Cherokee Springs	OC-TXH-001-B	125-500 μm
LL6	Chicora	OC-TXH-014-C	0-125 μm
LL6	Chicora	OC-TXH-014-B	125-500 μm
LL6	Bison	MB-TXH-089-A	0-63 μm
LL6	Bison	MB-TXH-089-B	63-125 μm
LL6	Dhurmsala	MB-TXH-090-A	0-63 μm
LL6	Dhurmsala	MB-TXH-090-B	63-125 μm
LL6	Nas	MB-TXH-091-A	0-63 μm
LL6	Nas	MB-TXH-091-B	63-125 μm
LL6	Y-74646	MB-TXH-085-A	0-25 μm
LL6	Y-74646	MB-TXH-085-B	25-45 μm
LL6	Y-74646	MB-TXH-085-C	45-75 μm

Notes. [(a)]Spectrum IDs with the "MJG" prefix are from the C-TAPE database, while all other spectra are from the RELAB database. All spectra were measured at a phase angle of 30°. All samples were measured at room temperature, except for the two C-TAPE spectra MJG 210 and MJG 203, for which the temperature was not reported.

Appendix B: Meteorite parameters

Table B.1: Meteorites used in this study and their band parameter.

Type	Sample name	BAR	BIC	BIIC[a]	Band I slope[b]	Band I depth	Band I width[c]	Band II slope[b]	Band II depth	Band II width[c]
H4	Avanhandava	0.767	0.9234	1.8951	0.007	0.145	0.76	-0.014	0.065	0.88
H4	Conquista	0.639	0.9239	1.9429	0.030	0.161	0.63	-0.021	0.060	0.88
H4	Farmville	0.625	0.9208	1.9221	0.003	0.167	0.77	-0.014	0.064	0.89
H4	Forest Vale	0.509	0.9266	1.8625	0.008	0.133	0.8	0.000	0.047	0.85
H4	Kabo	0.752	0.9249	1.8792	0.004	0.156	0.75	-0.003	0.066	0.92
H4	Marilia	0.690	0.9207	1.9461	0.010	0.178	0.73	-0.020	0.073	0.9
H4	Monroe	0.609	0.9231	1.9342	0.008	0.173	0.76	-0.017	0.072	0.885
H4	Ochansk	0.677	0.9238	1.9361	-0.009	0.199	0.77	-0.025	0.092	0.9
H4	São Jose do Rio Preto	0.889	0.9244	1.8554	0.005	0.177	0.74	-0.016	0.087	0.91
H5	Allegan	0.979	0.922	1.913	0.007	0.235	0.72	-0.015	0.124	0.92
H5	Ehole	0.875	0.9231	1.9424	0.002	0.273	0.79	-0.004	0.158	0.89
H5	Itapicuru-Mirim	0.688	0.9247	1.8893	0.004	0.209	0.71	-0.024	0.091	0.9
H5	Lost City	0.720	0.9245	1.9187	0.000	0.174	0.74	-0.024	0.075	0.89
H5	Macau	0.616	0.9267	1.9374	0.010	0.152	0.71	-0.020	0.060	0.89
H5	Pribram	0.716	0.9256	1.8849	0.014	0.197	0.73	0.005	0.087	0.92
H5	*Pultusk*	0.760	0.9281	1.9225	-0.001	0.203	0.76	-0.022	0.098	0.89
H5	Schenectady	0.691	0.9213	1.92	0.027	0.264	0.76	-0.002	0.112	0.88
H5	Uberaba	0.724	0.9311	1.9205	0.012	0.190	0.72	-0.018	0.081	0.91
H6	Andura	0.742	0.9156	1.8877	0.023	0.167	0.71	-0.003	0.069	0.91
H6	Butsura	0.710	0.9198	1.8935	-0.004	0.145	0.74	-0.014	0.062	0.92
H6	Canon City	0.647	0.9325	1.9203	0.006	0.441	0.78	-0.005	0.201	0.9
H6	Chiang Khan	0.759	0.9278	1.8987	0.002	0.287	0.76	-0.019	0.138	0.91
H6	Guarena	0.655	0.9204	1.8736	-0.002	0.349	0.76	0.000	0.169	0.93
H6	Ipiranga	0.732	0.9253	1.9001	0.008	0.196	0.73	-0.013	0.084	0.9
H6	Kernouve	0.677	0.9276	1.9018	-0.005	0.402	0.77	-0.006	0.185	0.925
H6	*Portales Valley*	0.538	0.9392	1.8917	0.018	0.304	0.77	0.006	0.119	0.9
L4	Atarra	0.568	0.9232	1.925	0.000	0.265	0.78	-0.015	0.122	0.87
L4	*Bald Mountain*	0.681	0.9161	1.9706	0.017	0.119	0.75	0.004	0.049	0.86
L4	Barratta	0.559	0.9241	1.9317	0.003	0.132	0.755	-0.008	0.054	0.875
L4	Rio Negro	0.646	0.931	1.8675	0.010	0.232	0.77	-0.009	0.101	0.87
L4	Rupota	0.551	0.9333	1.9677	-0.001	0.102	0.78	-0.008	0.040	0.86
L5	*Ausson*	0.926	0.922	1.9151	0.007	0.247	0.72	-0.019	0.129	0.92
L5	Blackwell	0.470	0.9354	1.9518	0.031	0.123	0.73	-0.009	0.051	0.83
L5	Cilimus	0.472	0.9286	1.9253	0.010	0.206	0.82	0.011	0.074	0.87
L5	Elenovka	0.507	0.9368	1.9251	0.002	0.356	0.815	-0.006	0.142	0.885
L5	*Ergheo*	0.524	0.9522	1.9384	0.019	0.222	0.765	-0.011	0.109	0.845
L5	Guibga	0.543	0.9334	1.923	0.008	0.259	0.79	-0.008	0.101	0.88
L5	Homestead	0.610	0.9299	1.9398	0.017	0.182	0.75	-0.017	0.077	0.87
L5	Mabwe-Khoywa	0.618	0.9289	1.9303	0.005	0.226	0.76	-0.001	0.103	0.89
L5	Malakal	0.509	0.9308	1.9367	0.012	0.206	0.79	0.005	0.075	0.87

Table B.1: Continued.

Type	Sample name	BAR	BIC	BIIC[a]	Band I slope[b]	Band I depth	Band I width[c]	Band II slope[b]	Band II depth	Band II width[c]
L5	Messina	0.498	0.9314	1.9232	0.006	0.188	0.79	-0.005	0.066	0.89
L5	Shelburne	0.576	0.9336	1.9315	0.005	0.289	0.78	-0.018	0.122	0.88
L5	Tsarev	0.604	0.94	1.9483	-0.001	0.151	0.765	0.000	0.062	0.915
L6	Air	0.454	0.9346	1.9234	0.006	0.161	0.79	-0.001	0.054	0.86
L6	Apt	0.430	0.9361	1.9355	0.010	0.314	0.81	0.001	0.108	0.86
L6	Aumale	0.523	0.9336	1.9352	0.014	0.301	0.81	0.004	0.123	0.86
L6	Bath Furnace	0.486	0.9331	1.9363	0.004	0.203	0.78	-0.017	0.074	0.87
L6	Chantonnay	0.437	0.9278	1.8784	0.006	0.120	0.88	0.004	0.039	0.78
L6	*Chateau Renard*	0.379	0.9482	1.9364	0.007	0.295	0.83	-0.011	0.100	0.855
L6	Denver	0.497	0.9366	1.9441	0.002	0.164	0.79	-0.017	0.060	0.87
L6	Girgenti	0.455	0.9363	1.9401	0.012	0.390	0.83	0.013	0.147	0.87
L6	*Harleton*	0.365	0.9491	1.9594	0.016	0.331	0.835	-0.004	0.107	0.86
L6	Karkh	0.355	0.9392	1.8956	0.001	0.142	0.81	0.001	0.039	0.87
L6	Kunashak	0.455	0.943	1.9308	0.011	0.302	0.81	0.008	0.109	0.87
L6	Kuttippuram	0.486	0.932	1.8857	0.004	0.232	0.84	0.005	0.086	0.85
L6	Kyushu	0.470	0.9413	1.9257	0.030	0.317	0.78	-0.006	0.114	0.87
L6	L'Aigle	0.714	0.9317	1.9445	-0.004	0.168	0.78	-0.030	0.077	0.88
L6	New Concord	0.515	0.9342	1.923	0.007	0.315	0.8	0.008	0.123	0.88
L6	Paranaiba	0.390	0.933	1.9511	0.019	0.121	0.77	0.007	0.032	0.9
L6	Patrimonio	0.573	0.9328	1.9403	0.007	0.264	0.79	-0.004	0.115	0.87
L6	Walters	0.440	0.9371	1.9145	-0.005	0.272	0.8	0.003	0.091	0.89
LL4	Benares(a)	0.413	1.0068	1.9643	0.031	0.199	0.8	-0.017	0.077	0.83
LL4	Greenwell Springs	0.406	0.9514	1.9479	0.023	0.271	0.82	-0.013	0.103	0.84
LL4	Hamlet	0.440	0.9407	1.9623	0.024	0.173	0.8	-0.010	0.066	0.85
LL4	*Soko-Banja*	0.369	0.9878	1.9666	0.016	0.311	0.84	-0.026	0.114	0.835
LL4	Witsand Farm	0.371	0.9966	1.9702	0.024	0.160	0.8	-0.020	0.056	0.81
LL5	Aldsworth	0.487	0.9399	1.95	0.013	0.166	0.8	-0.012	0.070	0.85
LL5	Alta'ameem	0.385	0.9519	1.9453	0.006	0.261	0.83	-0.013	0.091	0.85
LL5	Chelyabinsk	0.367	0.9513	1.9453	0.003	0.204	0.82	0.000	0.066	0.855
LL5	Olivenza	0.340	1.0037	1.9542	0.005	0.266	0.84	-0.025	0.087	0.83
LL5	Paragould	0.383	0.9569	1.9525	-0.006	0.176	0.82	-0.007	0.059	0.85
LL5	Tuxtuac	0.244	1.0316	1.9639	0.023	0.337	0.87	-0.013	0.088	0.8
LL6	Appley Bridge	0.256	1.0091	1.9486	-0.006	0.407	0.905	-0.008	0.109	0.815
LL6	Athens	0.195	1.0163	1.9331	-0.011	0.331	0.905	-0.001	0.072	0.825
LL6	Bandong	0.243	0.9897	1.9518	0.006	0.213	0.85	-0.002	0.051	0.84
LL6	Bensour	0.252	0.9934	1.9605	-0.006	0.237	0.87	-0.011	0.057	0.825
LL6	Cherokee Springs	0.353	0.9551	1.9211	-0.007	0.195	0.86	-0.010	0.061	0.83
LL6	Chicora	0.179	1.0103	1.9646	-0.006	0.272	0.915	0.001	0.054	0.8
LL6	Dhurmsala	0.494	0.9543	1.9392	-0.003	0.397	0.825	-0.018	0.175	0.86
LL6	Karatu	0.263	0.9987	1.9741	0.001	0.201	0.88	-0.004	0.050	0.81
LL6	Saint Séverin	0.251	0.9828	1.8806	0.013	0.185	0.87	0.021	0.047	0.84

Notes. [a]BIIC denotes the Band II center. [b]The units of Band I/II slope are μm^{-1}. [c]The units of Band I/II width are μm.

Appendix C: The exposure age of Didymos

Based on the cross-sectional areas of the primary and secondary, before the DART impact, Dimorphos contributed only about 4% of the total reflected light (Ieva et al. 2022). The pre-impact spectrum effectively represents the surface of the primary, therefore, to estimate the surface exposure age of the primary, we used the pre-impact spectrum (0926 spectrum) to calculate C_S. As described in Sect. 3.3, by de-reddening the Band I continuum slope of the pre-impact spectrum (0926 spectrum) of Didymos to the mean slope of ordinary chondrite spectra, a C_S value of −0.141 μm was obtained. The exposure age t of Didymos can be obtained from this C_S value using the weathering model proposed by Brunetto et al. (2006). Laboratory ion irradiation experiments on silicate materials have shown that when the ion fluence is below 10^{17} ions/cm^2, spectral reddening is primarily caused by atomic displacements within the silicate (Brunetto et al. 2006; Strazzulla et al. 2005; Brunetto & Strazzulla 2005). The damage parameter d refers to the number of displacements per unit area (displacements/cm^2), and its relationship with the C_S value (the damage curve) is given by

$$C_S = \alpha \ln(\beta d + 1), \tag{C.1}$$

where $\alpha = -0.33\ \mu$m, $\beta = 1.1 \times 10^{-19}$ cm^2. After the damage parameter d is obtained, the surface exposure age of the asteroid can be calculated using the following equation:

$$t = 2.53 \times 10^{-13} \left(\frac{D}{2.9\ \text{AU}}\right)^2 d, \tag{C.2}$$

where D is the semi-major axis of Didymos (1.64 AU). Substituting the C_S value of the 0926 spectrum into Eqs. (C.1) and (C.2) yields an exposure age of $t \sim 0.39$ Myr (Fig. C.1).

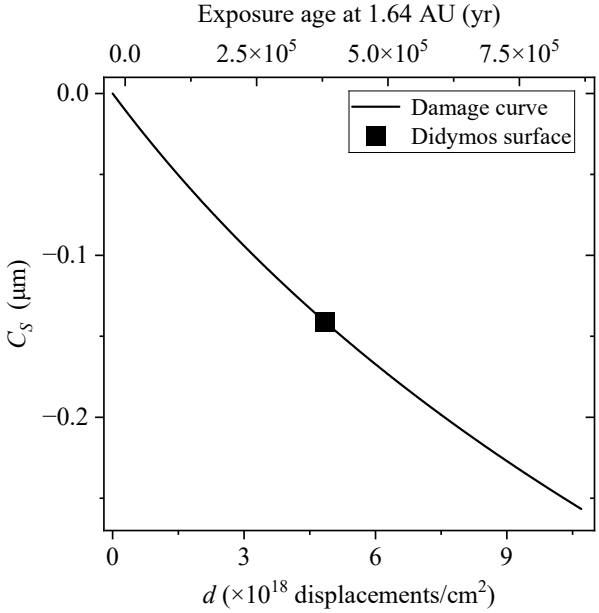

Fig. C.1: Damage curve and surface exposure age of Didymos. The top axis shows the corresponding surface exposure age at 1.64 AU, while the bottom axis shows the damage parameter d in 10^{18} displacements/cm^2, which is related to the top axis via Eq. (C.2). The black curve shows the relationship between the damage parameter d and C_S, as given by Eq. (C.1), and the black square indicates the measured C_S value of the Didymos surface, from which the surface exposure age is estimated.